

# Operational Inhomogeneities in $\text{La}_{0.9}\text{Sr}_{0.1}\text{Ga}_{0.8}\text{Mg}_{0.2}\text{O}_{3-\delta}$ Electrolytes and $\text{La}_{0.8}\text{Sr}_{0.2}\text{Cr}_{0.82}\text{Ru}_{0.18}\text{O}_{3-\delta}$ – $\text{Ce}_{0.9}\text{Gd}_{0.1}\text{O}_{2-\delta}$ Composite Anodes for Solid Oxide Fuel Cells

Y. Liao<sup>1\*</sup>, D. M. Bierschenk<sup>1</sup>, S. A. Barnett<sup>1</sup>, and L. D. Marks<sup>1</sup>

<sup>1</sup> Department of Materials Science and Engineering, 2220 Campus Drive, Northwestern University, Evanston, IL 60208, USA

Received November 2, 2010; accepted May 16, 2011

## Abstract

The electrolyte/anode interface in solid oxide fuel cells with  $\text{La}_{0.9}\text{Sr}_{0.1}\text{Ga}_{0.8}\text{Mg}_{0.2}\text{O}_{3-\delta}$  electrolytes and composite anodes containing  $\text{La}_{0.8}\text{Sr}_{0.2}\text{Cr}_{0.82}\text{Ru}_{0.18}\text{O}_{3-\delta}$  and  $\text{Ce}_{0.9}\text{Gd}_{0.1}\text{O}_{2-\delta}$  (GDC) was studied using transmission electron microscope Z-contrast imaging and energy dispersive X-ray spectroscopy. The anode/electrolyte interface of an operated cell had numerous defective regions in the electrolyte, immediately adjacent to anode GDC particles. These areas had a different chemical composition than other electrolyte regions and were crystallographically inhomogeneous. These

regions were not observed in a cell reduced in hydrogen that was not operated, suggesting that they were the result of combined electrical and chemical potential gradients present during cell operation. Ru nanoparticles were observed on the chromite surfaces of the operated.

**Keywords:** Catalyst, Chromite Anode, Degradation, Interface, LSGM Electrolyte, Microstructure, Nano, Ruthenium, SOFC, TEM

## 1 Introduction

Ni cermet anodes are commonly used in solid oxide fuel cells (SOFCs) [1–4], but there has been considerable interest in alternative oxide-based anodes [5]. The motivation for the alternative materials is to avoid problems with the Ni-based anodes, including susceptibility to coking in hydrocarbon and CO-rich fuels [6], poisoning by sulfur [7] and other fuel impurities [8], and degradation due to redox cycling [9]. A number of oxide materials have been identified that address these problems [10]. One recent example is  $\text{La}_{0.8}\text{Sr}_{0.2}\text{Cr}_{0.82}\text{Ru}_{0.18}\text{O}_{3-\delta}$  (LSCrRu). This material has yielded good electrochemical performance that appears to be related to the formation of Ru nanoparticles on the chromite surfaces, although this has only been verified in powders, not in the anodes themselves [11].

One of the problems with oxide anode materials is their incompatibility with the electrolyte. For example, there are

well-known problems with reactions between perovskite electrodes and yttrium-stabilized zirconia (YSZ) electrolytes that form resistive zirconate phases [12]. However, relatively little is known about the compatibility of oxide anodes with  $\text{La}_{0.9}\text{Sr}_{0.1}\text{Ga}_{0.8}\text{Mg}_{0.2}\text{O}_3$  (LSGM) electrolytes. A number of SOFCs with oxide anodes on LSGM-electrolyte supports have been reported [10, 11], and in some cases it was found that a La-doped ceria (LDC) interlayer was required to obtain good cell performance. The ceria interlayer presumably prevented deleterious anode/electrolyte interactions. However, little structural/chemical information is available for these material combinations [11].

Here we describe a transmission electron microscopy (TEM), scanning transmission electron microscopy (STEM), and energy dispersive X-ray spectroscopy (EDX) study of

[\*] Corresponding author, [yougui.liao@globalsino.com](mailto:yougui.liao@globalsino.com)

oxide-anode SOFCs, specifically the region near the interfaces between the LSCrRu anode and LSGM electrolyte. The as-prepared cell showed no unusual features. After exposure to fuel, the anode surfaces were decorated with Ru nanoparticles. In addition, SOFCs, operated with a current, exhibited new “defective” regions in the LSGM electrolyte near the anode–electrolyte interface; by defective, we mean here and throughout the paper, areas which have a different chemical composition than other electrolyte regions and were crystallographically inhomogeneous.

## 2 Experimental

Electrolyte supported SOFCs were fabricated similar to the devices previously described [11, 13]. LSGM was prepared by a solid state reaction: appropriate quantities of  $\text{La}_2\text{O}_3$ ,  $\text{SrCO}_3$ , and  $\text{Ga}_2\text{O}_3$  and  $\text{MgO}$  were mixed in ethanol, dried, and calcined at  $1,250\text{ }^\circ\text{C}$ . The resulting material was pulverized, wet ball-milled with poly vinyl buteral (PVB), dried, sieved, and uniaxially pressed into 19 mm diameter pellets that were sintered for 6 h at  $1,450\text{ }^\circ\text{C}$ .

The composite anodes were prepared with 50 wt.-% LSCrRu and 50 wt.-%  $\text{Ce}_{0.9}\text{Gd}_{0.1}\text{O}_{2-\delta}$  (GDC, Fuel Cell Materials) as described previously [11] and summarized briefly here. The ionic conductor GDC was added to the LSCrRu as it was previously shown to improve electrochemical performance [11]. The LSCrRu was prepared by ball-milling  $\text{La}_2\text{O}_3$ ,  $\text{SrCO}_3$ ,  $\text{Cr}_2\text{O}_3$ , and  $\text{RuO}_2$  in water. The slurry was then dried and calcined at  $1,200\text{ }^\circ\text{C}$  for 3 h. The phase purity of the powder was confirmed by X-ray diffraction. The resulting powder was mixed with GDC (50 wt.-%) via ball-milling, dried, sieved, and suspended in a vehicle (Heraeus, V-737) to form an ink. In a similar fashion  $\text{La}_{0.8}\text{Sr}_{0.2}\text{CrO}_{3-\delta}$  (LSCr) was synthesized by a solid state reaction and prepared as an ink. The LSCrRu–GDC ink was then applied by screen printing to the LSGM pellets. After this layer was dried, a layer of LSCr was applied using screen printing as a current collector. The layers were then co-fired at  $1,200\text{ }^\circ\text{C}$  for 3 h.

Thick film cathodes consisting of 50 wt.-%  $\text{La}_{0.6}\text{Sr}_{0.4}\text{Co}_{0.2}\text{Fe}_{0.8}\text{O}_{3-\delta}$  (LSCF Praxair)–50 wt.-% GDC and a pure LSCF current collector were prepared and applied to the electrolyte in a similar fashion as the anode. The cathode layers were co-fired at  $1,000\text{ }^\circ\text{C}$  for 3 h. The cathode and anode areas were both  $0.5\text{ cm}^2$  and defined the active area of the cells. The resulting structure had the form:  $\sim 30\text{ }\mu\text{m}$  LSCF/ $\sim 30\text{ }\mu\text{m}$  LSCF–GDC/ $\sim 300\text{ }\mu\text{m}$  LSGM/ $15\text{ }\mu\text{m}$  LSCrRu–GDC/ $10\text{ }\mu\text{m}$  LSCr.

For electrical testing, Au (Heraeus C5756) current collector grids were applied to both electrodes. Electrical contacts were made with Ag wire and Ag paste (DAD-87 Shanghai Research Institute of Synthetic Resins) and the cell was mounted for testing in an alumina tube. The cathode was open to stagnant lab air. Impedance spectra and potential *versus* current density

curves were periodically recorded with a Zahner IM-6 electrochemical workstation to monitor the break-in behavior of the cell. The cell polarization resistance ( $R_p$ ) was estimated as the difference between the low frequency and high frequency real-axis intercepts on a Nyquist plot. During operation, the cell voltage was maintained near 0.5 V, except while recording impedance spectra and current–voltage characteristics.

TEM samples were prepared by mounting the fuel cells in epoxy. Three cells with different histories were studied. One cell was operated in dry  $\text{H}_2$  for 117 h at  $800\text{ }^\circ\text{C}$  (the cell was briefly cooled to  $600\text{ }^\circ\text{C}$  during electrical testing). The open circuit potential of this cell varied between 1.06 and 1.10 V at  $800\text{ }^\circ\text{C}$ , corresponding to oxygen partial pressures of  $3 \times 10^{-21}$ – $5 \times 10^{-22}$  atm. A second cell was reduced for 120 h in 3%  $\text{H}_2\text{O}/97\% \text{H}_2$  at  $800\text{ }^\circ\text{C}$ . This composition gave an oxygen partial pressure of  $4.5 \times 10^{-22}$  atm, similar to the calculated  $p(\text{O}_2)$  in the anode of the operated cell. A baseline cell was kept in the as-prepared state. The history of these cells is summarized in Table 1. A thin section was milled and lifted from each cell in an FEI Helios NanoLab 600i dual beam focused ion beam (FIB) system. Figure 1 shows a typical cell section—the dense electrolyte is on the left and the porous anode is on the right. In order to minimize Ga deposition and

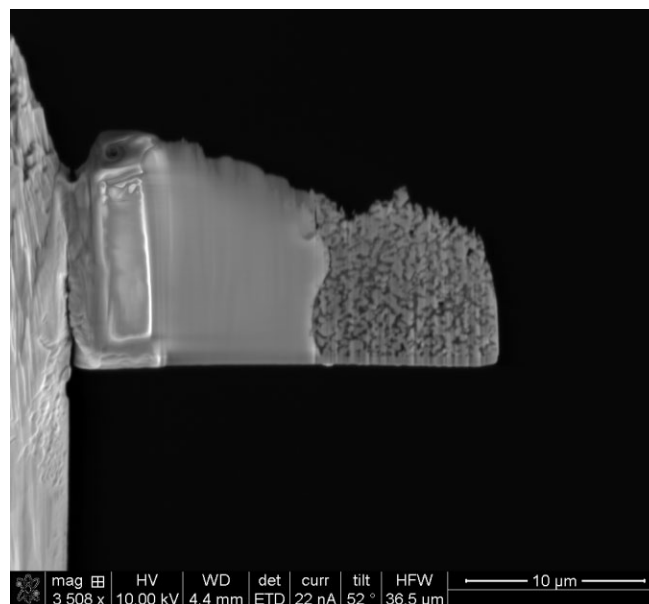


Fig. 1 Scanning electron micrograph of a typical TEM sample.

Table 1 Summary of the sample history for the as-prepared, reduced, and operated cell.

Sample	Fuel	$P(\text{O}_2)$ / atm	Temperature / $^\circ\text{C}$	Duration / h	Notes
As-prepared	N/A	N/A	N/A	N/A	Cell was not operated
Reduced	3% $\text{H}_2\text{O}/97\%\text{H}_2$	$4.5 \times 10^{-22}$	800	120	
Operated	100% $\text{H}_2$ (dry)	$3 \times 10^{-21}$ – $5 \times 10^{-22}$	800	117	Cell operated near 0.5 V, except during measurements

contamination, the ion beam was aligned parallel to the surface being milled. During the final milling step, the beam was maintained at a high voltage (30 keV) and a low current (16 pA) [14]. The samples were studied using Z-contrast and EDX in a JEOL 2100 system, operating at 200 kV. The spot size of the electron beam used for EDX measurements was  $\sim 1$  nm. Both EDX imaging and line-scan compositional profiles were used to examine the nature of the interfaces before and after cell operation.

### 3 Results

#### 3.1 Cell Performance

The cell break-in behavior was captured by periodically measuring the cell impedance. Figure 2 shows the Bode and Nyquist plots of impedance spectra recorded after 26, 47, 75, and 117 h of operation in dry  $H_2$  at 800 °C.  $R_p$  decreased during the first 75 h of testing, and then stabilized at  $\sim 0.3 \Omega \text{ cm}^2$ . In a separate test the cathode  $R_p$  was measured in an LSCF/LSCF-GDC/LSGM/LSCF-GDC/LSCF symmetric cell and was  $0.02 \Omega \text{ cm}^2$  at 800 °C, indicating that  $R_p$  was primarily due to the anode. The ohmic resistance of the cell did not change appreciably during testing. Prior studies reported a slight increase in the ohmic resistance and a stable cathode resistance during operation [11, 13]. Figure 3 shows the current voltage characteristics at 26 h. For comparison, the stabilized performance is shown after 117 h of operation the peak power density was  $400 \text{ mW cm}^{-2}$ . The above results are consistent with prior reports for LSCrRu-GDC anodes [11, 13].

#### 3.2 LSCrRu-GDC Anode

Anode cross-sections prepared by the FIB lift-out technique were studied. High-resolution images and electron diffraction patterns (not shown) indicated that the anode oxide phases showed the expected crystal structures in both the as-prepared and operated cells. While the as-prepared cell did not show any evidence of Ru particle formation, Ru nanoparticles were observed on LSCrRu grains at the anode/electrolyte interface in the operated anode as shown in Figure 4. It was confirmed using EDX that the nanoparticles were Ru. The mean diameter of Ru nanoparticles near the electrolyte

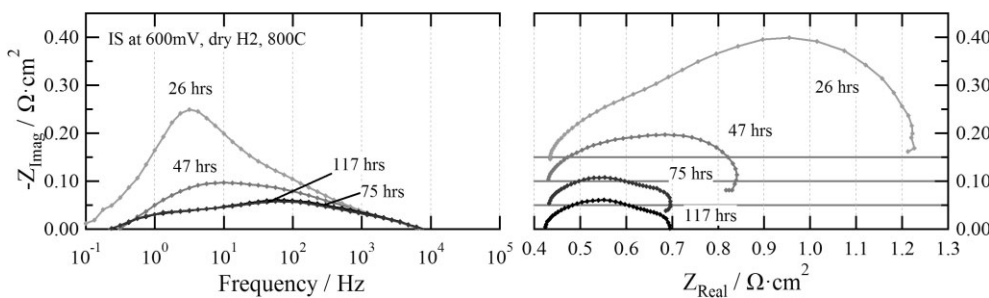


Fig. 2 Impedance Bode (left) and Nyquist (right) for the cell operated at 800 °C after 26, 47, 75, and 117 h of operation.

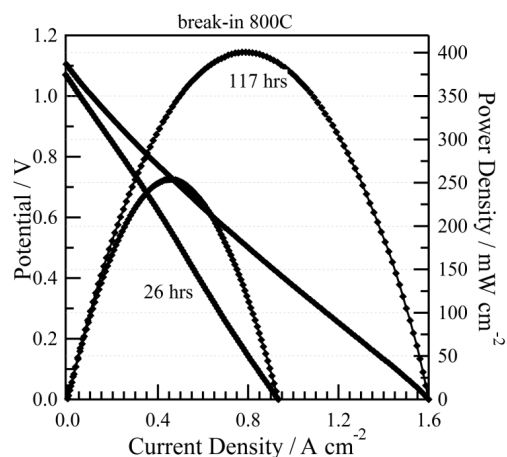


Fig. 3 Cell potential and power density vs. current density after operation for 26 and 117 h.

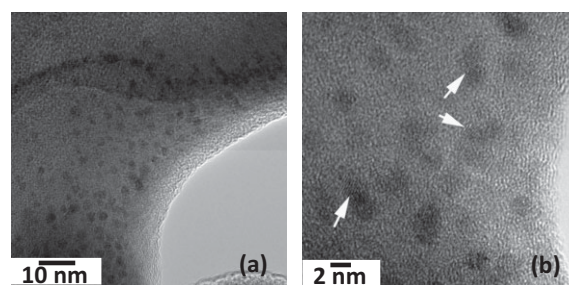


Fig. 4 TEM images in (a) and (b) show Ru nanoparticles formed in the operated cell. The high-resolution TEM image (b) reveals the crystalline phase of Ru particles, marked by the white arrows.

was  $\sim 2.9$  nm. While this is the first observation of nanoparticle formation in operated SOFCs, the results are quite similar to observations on LSCrRu powders that had been exposed to  $H_2$  fuel [11].

#### 3.3 Anode-Electrolyte Interface

Figure 5 shows a TEM image taken from the reduced cell. The anode/electrolyte interface was relatively flat, with the anode grains typically 300–800 nm in diameter. Low-magnification survey TEM images were also taken to ensure that the smaller region shown in Figure 5 was representative. As shown in Figure 6a, the as-prepared cell showed results very similar to those in Figure 5. The operated cells (Figure 6c) were found to have numerous inhomogeneities in the LSGM electrolyte at the LSGM/anode interface. These defects usually occurred directly adjacent to locations where anode GDC

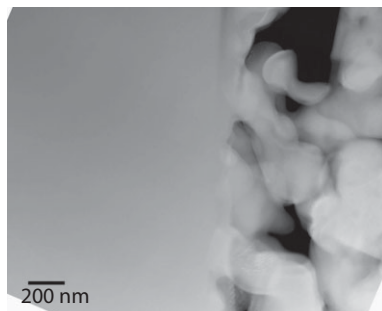


Fig. 5 Typical Z-contrast image taken from the as-prepared fuel cell, showing morphology of interface between GDC/LSCrRu anode (right) and electrolyte (left).

particles were in contact with the LSGM. In Section 3.3.1, two such interfacial locations are examined in detail. Section 3.3.2 shows, for comparison, a region where an anode LSCrRu particle was in contact with LSGM.

### 3.3.1 GDC in Contact with LSGM

Figure 6 shows Z-contrast images of typical LSGM/GDC interfacial regions, along with EDX line-scan profiles, from the as-prepared and operated fuel cells. The electrolyte of the as-prepared fuel cell (Figure 6a) has variations in contrast near the anode that indicate some minor porosity. Figure 6b shows the elemental concentrations *versus* position relative to the interface; the scan was recorded along the line marked in the TEM images. The cation concentrations in the electrolyte were reasonably consistent with the expected elemental concentrations of the LSGM. However, the concentration of La in the ceria particle was elevated, although the high-La baseline concentration far from the interface may have been an artifact due to the close overlap between the La and Ce EDX peaks. The concentration of Ce decreased approaching the interface.

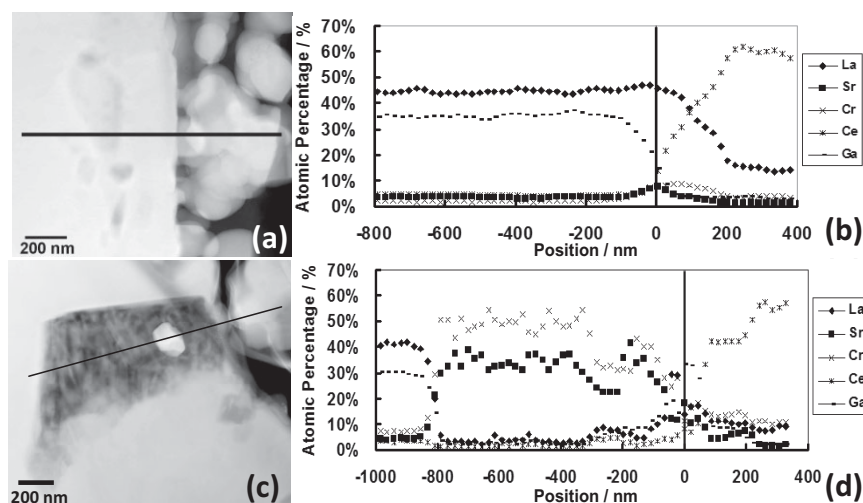


Fig. 6 Z-contrast image (a) and EDX compositional profile (b) from the electrolyte–anode interface regions of the as-prepared cell. Z-contrast image (c) and EDX compositional profile (d) are also shown for the operated cell. The lines in (a) and (c) indicate the locations of the line scans, which both went through a point where a GDC particle contacted the LSGM.

Some segregation of Sr and Cr at the interface was evident, but there was no significant accumulation of Ce, Gd, Ga, or Mg (not shown). There was a significant interfacial broadening over a range of 200–300 nm. Similar compositional variations were also seen in a few other areas tested, confirming that they were general and not just effects associated with a specific local structure.

Figure 6c shows a typical Z-contrast image taken from the operated fuel cell. Near the LSGM–GDC contact point, a  $\sim 500 \text{ nm} \times 1,000 \text{ nm}$  trapezoidal-shaped region in the LSGM electrolyte appeared darker than the surrounding electrolyte material. This feature was not unique to the image in Figure 6c, but was seen at every GDC–LSGM contact point. Furthermore, the size of the dark regions scaled with the adjacent GDC particle, suggesting a direct connection with the size of each particle. The contrast can be attributed (to first order) to a lower atomic mass density in the “defect” region than in the surrounding electrolyte. The darker region in Figure 6c also shows noticeable strain/diffraction contrast indicating that it contains crystallographic defects and is not a single crystal region. Figure 6d shows the corresponding EDX line scan. Outside of the dark region, the La/Sr and Ga/Mg ratios, along with the A/B site ratio, matched the expected ratio for LSGM. Within the dark region, the concentrations of La and Ga were lower than expected, while the concentrations of Cr and Sr were elevated.

Another region observed from the operated cell is shown in Figure 7a. EDX element maps in Figures 7b–f shows the distribution of La, Sr, Ga, Cr, and Ce at the anode/electrolyte interface. This portion of the anode contains both LSCrRu and GDC in close proximity to the electrolyte. A triangular-shaped region is present in the LSGM electrolyte (Figure 7a) that shows a mottled morphology with strain/diffraction contrast associated with crystallographic inhomogeneities that is similar to the trapezoidal defect observed in Figure 6c.

As shown in Figure 6, this region contains higher than expected concentrations of Sr and Cr and no detectable Ga. Note that some of the Ce signal in Figure 7f is an artifact due to peak overlap between Ce La and La La.

### 3.3.2 LSCrRu in Contact with LSGM

For the as-prepared fuel cell, the elemental profiles at the electrolyte surface in contact with an LSCrRu particle matched the expected stoichiometries for LSCrRu and LSGM. Figure 8a shows an image centered at the interface of an LSCrRu particle with the LSGM electrolyte. While there were small defects present in the LSGM electrolyte that were similar to those in the as-prepared cell (Figure 6a), there was nothing like the large defect adjacent to GDC particles

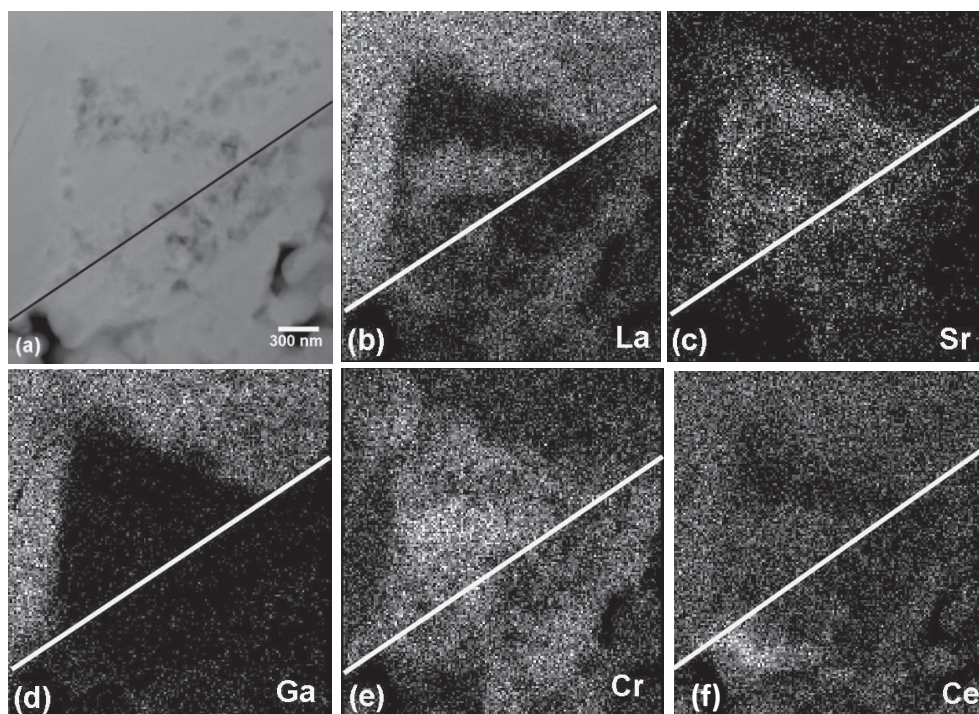


Fig. 7 Z-contrast image (a) and EDX maps for La (b), Sr (c), Ga (d), Cr (e), and Ce (f) at the anode/electrolyte interface of the operated SOFC. The diagonal line in the images indicates the approximate anode/electrolyte interface, with the electrolyte located above and to the left.

(Figure 6c). The expected La/Sr ratio was observed everywhere except near the anode/electrolyte interface due to Sr enrichment (Figure 8 b). The Ga/Mg ratio was lower than expected, perhaps indicating more out-diffusion of Ga. The A/B cation site ratios remained near 50:50 within experimental error.

## 4 Discussion

The above results show defective regions that formed near the LSGM/anode interface adjacent to anode GDC particles, after SOFC operation. The defects did not form during the anode firing/processing in air at 1,200 °C (as indicated by the as-prepared sample), nor after exposing the anode to fuel (as seen in the reduced sample), but rather when the anodes were exposed to fuel and the cell operated at a substantial current density at 800 °C. A few possible mechanisms of defect formation are suggested below.

The observation of defects in LSGM adjacent to GDC particles suggests that the interaction between LSGM and GDC must play an important role. Indeed, La diffused from LSGM into GDC during firing and the loss of La from LSGM likely contributes to de-stabilization of the perovskite phase, which exists over a relatively narrow composition range. Note that La loss occurs because GDC does not provide the high-La activity of LDC, which is sometimes used as a protective barrier layer with LSGM to avoid La loss and reactions with

anode materials [15–17]. The present case where GDC, LSCrRu, and pores were in contact with the LSGM is also different than prior work where LDC was a continuous layer separating the LSGM and anode. This is probably important given that the defect areas were enriched in Sr and Cr, which must have come from the adjacent LSCrRu phase.

As shown in Figure 4, LSCrRu is unstable under reducing conditions when Ru precipitates out in the form of nanoparticles on the oxide surface. While changes in the LSCrRu perovskite structure have not been observed during Ru precipitation [11], the perovskite structure is likely become unstable if enough Ru is lost to significantly change the A-to-B-site ratio. Such changes in LSCrRu might indirectly affect the interaction between LSGM and GDC. For example, it may make it easier for the chromite to supply the Sr and Cr that accumulates in the defect regions.

While the above effects probably play a role in producing the observed defects, they are alone not sufficient to explain them. It was only after cell operation with a current and with the anode under reducing conditions that the defects were observed. The present changes appear to result from a combination of the above-noted materials de-stabilization effects with gradients in oxygen chemical potential and electrical potential that are present during cell operation. It is known that morphological instabilities, kinetic decomposition, and kinetic demixing can occur in oxide materials under such gradients [18]. Gradients in the oxygen chemical potential,  $\mu_{\text{O}}$ , are present at the anode/electrolyte interface since the elec-

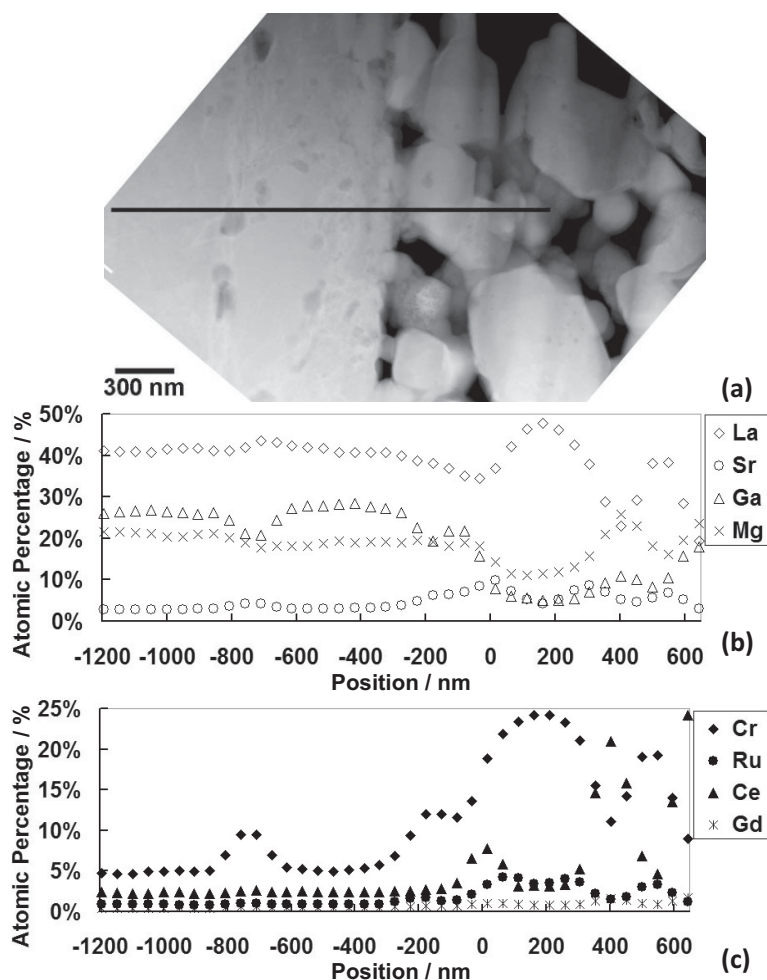


Fig. 8 Z-contrast micrograph from the operated fuel cell at the interface between the LSGM electrolyte (left) and the anode (right) centered at a location where a LSCrRu particle contacted the LSGM (a); The line in (a) represents the location of the EDX line profiles shown in (b) and (c).

trolyte is supplying oxygen to an anode that is immersed in hydrogen fuel. The oxygen chemical potential ( $\mu_{\text{O}}$ ) gradient gives rise to gradients of the cation chemical potentials ( $\mu_i$ ) as described by the Gibbs–Duhem equation [18]

$$\sum_i x_i d\mu_i + x_{\text{O}} d\mu_{\text{O}} = 0 \quad (1)$$

where the  $x$ 's are mole fractions. Strong electrical potential gradients are also present near the anode/electrolyte interface. The net gradient  $\nabla\eta_i$  driving motion of charged cations  $i$  includes both the chemical and electrical gradients [19, 20], as given by

$$\nabla\eta_i = \nabla\mu_i + z_i F \nabla\Phi \quad (2)$$

where  $z_i$  is the cation charge,  $F$  the Faraday's constant, and  $\Phi$  is the electric potential.

Although, cation diffusivities are normally several orders of magnitude lower than that of oxygen ions [21], at sufficiently long times, high temperatures [22], and electric fields

[23–25], substantial cation migration may still occur. Note that the migration of the different cations are not identical; certain elements migrate faster, others slower [26]. We can expect the appropriate gradient terms and concentration changes to be appreciable over a region of about 1  $\mu\text{m}$  from the interface [27], consistent with the experimental results.

The location of defects adjacent to GDC particles is probably due in part to the above-mentioned La loss from LSGM to GDC, which presumably helps to de-stabilize LSGM directly adjacent to GDC particles. Furthermore, the GDC network provides high-ionic conductivity paths for current flow, such that LSGM–GDC contact points presumably experience substantially higher oxygen ion current densities than the average cell value ( $\sim 1 \text{ A cm}^{-2}$ ). Locally high-current densities produce locally high-potential gradients, such that the above-mentioned electric-field effects will be exacerbated in the LSGM–GDC contact region. Detailed modeling, using structures similar to the experimentally observed morphologies rather than simplified model structures, would be required to verify the above hypothesis.

The LSGM electrolyte defects should cause an increase in cell ohmic resistance, although the increase may be quite small based on the small defect volume fraction compared to the  $\sim 500 \mu\text{m}$  thick electrolyte. The ohmic resistance of the operated cell (Figure 2) did not change appreciably during operation. However, similar cells with LSCrRu/GDC anodes showed an increase in ohmic resistance during testing [13] that might be explained by defect formation.

## 5 Summary and Conclusion

The anode/electrolyte interface regions were studied in LSGM electrolyte supported cells containing LSCrRu/GDC anodes with STEM using Z-contrast and EDX techniques. For an as-prepared cell, there was some interdiffusion of La into GDC along with slight segregation of Sr and Cr to the anode/electrolyte interface. Exposure of the anode to fuel resulted in nucleation of Ru nanoparticles on anode chromite surfaces, but no apparent changes at the interface. Cell operation with a current resulted in the appearance of extended defects in the LSGM electrolyte directly adjacent to anode GDC particles. These defects were depleted of Ga and La and enriched with Sr and Cr. The defects were also crystallographically inhomogeneous and were explained by the combined effects of electrical and chemical potential gradients present at the anode–electrolyte interface during cell operation. Localized changes in the anode composition that occurred during firing may have also contributed to defect formation. The defect regions had little apparent impact on cell performance.

Rather, the performance appeared to be dominated by the formation of Ru nanoparticles that decreased the LSCrRu anode polarization resistance..

## References

- [1] S. C. Singhal, *Solid State Ionics* **2000**, *135*, 305.
- [2] A. B. Stambouli, E. Traversa, *Renew. Sust. Energy Rev.* **2002**, *6*, 433.
- [3] N. P. Brandon, S. Skinner, B. C. H. Steele, *Annu. Rev. Mater. Res.* **2003**, *33*, 183.
- [4] S. M. Haile, *Adv. Mater. (Weinheim, Ger.)* **2003**, *51*, 5981.
- [5] B. D. Madsen, S. A. Barnett, *The influence of Ni Content on Ceramic-Based Solid Oxide Fuel Cell Anodes*, in *Solid Oxide Fuel Cells IX*, 2005. The Electrochemical Society Proceedings Series: The Electrochemical Society, Pennington, NJ, **2005**.
- [6] B. C. H. Steele, I. Kelly, H. Middleton, R. Rudkin, *Solid State Ionics* **1988**, *28–30*, 1547.
- [7] Y. Matsuzaki, I. Yasuda, *Solid State Ionics* **2000**, *132*, 271.
- [8] K. Haga, S. Adachi, Y. Shiratori, K. Itoh, K. Sasaki, *Solid State Ionics* **2008**, *179*, 1427.
- [9] P. Tanasini, M. Cannarozzo, P. Costamagna, A. Faes, J. VanHerle, A. Hessler-Wyser, C. Comninellis, *Fuel Cells* **2009**, *09*, 740.
- [10] H. U. Anderson, *Solid State Ionics* **1992**, *52*, 33.
- [11] W. Kobsiriphat, B. D. Madsen, Y. Wang, L. D. Marks, S. A. Barnett, *Solid State Ionics* **2009**, *180*, 257.
- [12] S. P. Simner, J. P. Shelton, M. D. Anderson, J. W. Stevenson, *Solid State Ionics* **2003**, *161*, 11.
- [13] B. D. Madsen, W. Kobsiriphat, Y. Wang, L. D. Marks, S. A. Barnett, *J. Power Sources* **2007**, *166*, 64.
- [14] Y. Liao, J.-Y. Degorce, J. Belisle, M. Meunier, *J. Electrochem. Soc.* **2006**, *153*, G16.
- [15] K. Huang, J.-H. Wan, J. B. Goodenough, *J. Electrochem. Soc.* **2001**, *148*, A788–A794.
- [16] Y. Lin, S. A. Barnett, *Electrochem. Solid-State Lett.* **2006**, *9*, A285.
- [17] Z. Bi, Y. Dong, M. Cheng, B. Yi, *J. Power Sources* **2006**, *161*, 34.
- [18] M. Martin, *J. Chem. Thermodyn.* **2003**, *35*, 1291.
- [19] S. R. de Groot, P. Mazur, *Non-Equilibrium Thermodynamics*, North-Holland, Amsterdam, **1962**, 510.
- [20] J. Janek, C. Korte, *Solid State Ionics* **1999**, *116*, 181.
- [21] P. Kofstad, *Nonstoichiometry, Diffusion and Electrical Conductivity in Binary Metal Oxides*, Wiley, New York, **1972**, 121.
- [22] J. Wolfenstine, *Solid State Ionics* **1999**, *126*, 293.
- [23] G. Petot-Ervas, C. Petot, *Solid State Ionics* **1998**, *4*, 336.
- [24] D. Monceau, M. Filal, M. Tcbtoub, C. Petot, G. Petot-Ervas, *Solid State Ionics* **1994**, *73*, 221.
- [25] P. Ruello, A. Rizea, C. Petot, G. Petot-Ervas, M. J. Graham, G. I. Sproule, *Solid State Ionics* **2001**, *7*, 81.
- [26] H. Schmalzried, W. Laqua, P. L. Lin, *Naturforschung* **1979**, *34a*, 192.
- [27] K. T. Jacob, A. K. Shukla, *J. Mater. Res.* **1987**, *2*, 338.